AIAA JOURNAL
Vol. 45, No. 8, August 2007

Unsteady Flowfield Around Tandem Cylinders as Prototype Component Interaction in Airframe Noise

Mehdi R. Khorrami,* Meelan M. Choudhari,* David P. Lockard,† Luther N. Jenkins,‡ and Catherine B. McGinley‡
NASA Langley Research Center, Hampton, Virginia 23681-2199

DOI: 10.2514/1.23690

The current effort characterizes the details of flow interactions and wake interference effects between two cylinders in a tandem configuration. This setup is representative of several component-level flow interactions that occur when air flows over the main landing gear of aircraft. Such interactions are likely to have a significant impact on the noise radiation associated with the undercarriage. This paper focuses on two-dimensional, time-accurate flow simulations of two distinct tandem cylinder flow regimes, associated with short and intermediate separation distances between the two cylinders. Unsteady Reynolds averaged Navier–Stokes simulations using a two-equation turbulence model run at a Reynolds number of 1.66×10^5 and a Mach number of 0.166 are presented. Emphasis is placed on understanding both the time-averaged and unsteady flow features between the two cylinders and in the wake of the rear cylinder. Predicted mean-flow quantities and vortex shedding frequencies show reasonable agreement with measured data for both cylinder spacings. Computations for the short separation distance exhibit a nonphysical decay of flow unsteadiness with time; however, the predicted sensitivity of the mean lift coefficient to small variations in the upstream flow angularity explains the asymmetric flowfield observed in the present and previous measurements.

Introduction

AIRFRAME noise constitutes a major component of the total aircraft noise during approach and landing. For medium and large civil transports, a significant portion of the airframe noise can be attributed to the landing gear, especially the main landing gear. The proximity of many bluff bodies of various sizes and shapes that collectively make up the main landing gear produce an extremely complex flowfield that is highly interactive and nonlinear in nature. Physics-based modeling of landing-gear noise requires a fundamental understanding of the unsteady flow interactions between the various components. A canonical configuration that models a variety of component-level interactions is that of multiple cylinders with axes parallel to each other. The wheels, axles, and brake pistons involve cylinderlike shapes of similar size, whereas the combination of the main strut and the hydraulic lines involves interactions between cylinders of disparate scales. The present paper is focused on the case of similar size tandem cylinders. Configurations of cylinders of disparate diameters are currently under consideration and will be reported in future papers.

The case of a tandem cylinder configuration has been considered before. Zdravkovich [1] and Ohya et al. [2] provide a detailed review of the previous work. Although informative, the majority of the past studies were restricted to flows where the Reynolds number (Re) was in the low subcritical flow regime [1–9], that is, dominated by laminar flow separation and periodic vortex shedding. According to [1–3], several distinct flow regimes have been observed in such flows. The three most prominent correspond to short, intermediate, and large separation distances between the cylinders' centerlines. In the case of short separations ($L/D < 2.4$, where D is the diameter and L is the distance between the two centers), the two cylinders behave as a single bluff body with vortex shedding occurring at the rear cylinder only. For large separation distances, the flowfield approaches that of an isolated single cylinder. At intermediate (critical) separation distances, the flow is bistable, switching intermittently between the flow states corresponding to short and large separation distances.

Measuring surface pressure fluctuations and using smoke flow visualization, Igarashi [4,5] found additional flow patterns that are a subset of the three main regimes discussed previously. For separation distances of $1.1 < L/D < 2.0$, the gap flow was found to depend on the Reynolds number, thus affecting the shedding frequency. Ljungkrona and Sunden [7] also reported a similar Reynolds number dependency. The effects of freestream turbulence on the tandem cylinder flow field were studied by Ljungkrona et al. [6] who found the critical spacing decreased with increasing turbulence intensity. As pointed out by the authors, a higher turbulence intensity produces effects that are similar (but not identical) to increasing the Reynolds number. That is, it alters the state of the boundary layer and thus the nature of flow separation experienced by the front cylinder. Using hot-wire anemometry and pressure probes, velocity and pressure fluctuations in the wake of the cylinders were measured by Wu et al. [8]. They observed increasing spanwise coherence with decreasing separation distance. For $L/D < 3.0$, the magnitude of the coherence always turned out to be higher than the case of a single cylinder. Overall, as noted by the authors, the magnitude of the spanwise coherence depends on the gap spacing and the Reynolds number.

To the best of our knowledge, Lin et al. [9] provided the only detailed off-surface flow measurements for the tandem cylinder configuration. Using particle image velocimetry (PIV), the flowfield within the gap and in the wake of the rear cylinder for several separation distances was mapped at $Re = 1.0 \times 10^4$. It was observed that the separated shear layer from the front cylinder exhibits the presence of Kelvin–Helmholtz (KH) instabilities (vortices) which in turn influence flow separation from the downstream cylinder.

Investigation of the tandem cylinder flowfield and wake interference effects at high Reynolds numbers were performed by Okajima [10], Arie et al. [11], Sun et al. [12], Gu et al. [13], Gu [14], and Gu and Sun [15]. Okajima [10] performed extensive measurements to determine the effects of Reynolds number variation on the flowfield. Drag and vortex shedding frequencies for

Presented as Paper 2866 at the 11th AIAA/CEAS Aeroacoustics Conference, Monterey, California, 23–25 May 2005; received 6 March 2006; revision received 15 February 2007; accepted for publication 25 February 2007.

*Aerospace Technologist, Computational Aerosciences Branch. Associate Fellow AIAA.
†Aerospace Technologist, Computational Aerosciences Branch. Senior Member AIAA.
‡Aerospace Technologist, Flow Physics and Control Branch.

the individual cylinders were measured over the Reynolds number ranging from subcritical to supercritical regimes. However, no mean or fluctuating surface pressure measurements were obtained. Three distinct cases were considered: smooth cylinders, a locally roughened front cylinder, and a fully roughened front cylinder. Although the critical Reynolds number was reduced significantly, the critical spacing L/D was found to be somewhat fixed between 3.5 and 3.8 for all three surface finishes. Surface pressure fluctuations at upper subcritical Reynolds number (1.57×10^4) were obtained by Arie et al. [11]. Based on their measurements, for $L/D < 7.0$, the root-mean-square (rms) drag and lift associated with the rear cylinder is larger than those for the front cylinder. The rms pressure distribution on the rear cylinder has multiple peaks with the highest distribution occurring at a separation slightly larger than the critical spacing. Surface pressure fluctuations and mean pressure distributions at very high subcritical and supercritical Reynolds numbers were measured by Gu and coworkers [12–15]. According to [12], the rms pressure amplitude at supercritical Reynolds number is noticeably lower than those associated with subcritical Reynolds numbers, demonstrating a weakening of the wake interference effects. In addition, at higher Reynolds number, the rms pressure distribution on the rear cylinder shows a more prominent dual peak structure [13].

An unexplained feature of the tandem cylinder configuration, at separation distances below critical spacing, is the observed asymmetry in the mean surface pressure distribution. In particular, the asymmetry becomes more pronounced for separations $L/D < 2.0$. Based on their measurements at $Re = 2.0 \times 10^4$, Ljungkrona et al. [6] attributed the existing asymmetry to small deflections in the tandem arrangement but have stated that despite their genuine effort, they were not always able to maintain a symmetrical pressure distribution. Measurements by Gu [14] revealed that the asymmetry in pressure at small gaps is persistent even at supercritical Reynolds numbers although no explanation or discussion of the underlying cause was provided by the author. The flow asymmetry was corroborated by the PIV measurements of [9] that clearly shows the presence of asymmetrical bias within the gap despite geometrical symmetry of the configuration. Similar asymmetrical tendencies were also observed during execution of the current measurements. These tendencies will be discussed in a later section where targeted computations are used to provide a plausible explanation for the flow asymmetry.

Compared to the level of experimental efforts, computational simulation of the tandem cylinder configuration has received less attention in the past. Most previous studies were limited to Reynolds numbers (e.g., see [16–18]) less than 2.0×10^4 and therefore the results are not fully appropriate for the aeroacoustic problems of interest.

Despite their usefulness, the earlier experiments lack simultaneous on-surface and off-surface measurements that are needed for benchmarking the computations and enabling physics-based models for sound radiation. The present computational effort is part of a synergistic combination of experiments and flow simulations that is aimed at providing a holistic view of the tandem cylinder flowfield at sufficiently large Reynolds numbers. Separation distances of $L/D = 1.435$ and 3.7 (representing two of the three possible flow regimes observed in earlier experiments) were chosen for this joint study. The experimental effort was conducted in the basic aerodynamic research tunnel (BART) at NASA Langley Research Center (LaRC). The ease of optical access at BART allowed detailed measurements of the flowfield using the PIV technique. Moreover, extensive measurements in the wake of the rear cylinder were conducted using hot-wire probes to obtain the frequency content and two-point correlations within the unsteady flowfield.

The experiments were conducted at a Reynolds number of $Re = 1.66 \times 10^5$ based on the cylinder diameter and the maximum tunnel speed of $M = 0.166$. To ensure turbulent flow separation, the boundary layer on the front cylinder was tripped between azimuthal locations of 50 and 60 deg on either side of the leading stagnation point. The measured surface pressure distribution for the large separation case was nearly identical to that measured by previous investigators for a single, isolated cylinder at a Reynolds number greater than 8×10^6. Details of the measurements conducted in BART are discussed in a separate paper by Jenkins, Khorrami, Choudhari, and McGinley [19] (hereafter referred to as JKCM). A portion of their measurements will be used here for comparison purposes to judge the accuracy and shortcomings of the present computations.

This paper is organized as follows. After the Introduction, a brief description of the computational methodology will follow whereby the flow solver, tandem geometry, and the topology of the generated mesh are discussed. The remainder of the paper is devoted to the presentation of the computed flowfields and their comparison with measurements. A complete discussion of the mean and rms surface pressure distributions is provided first, followed by presentation of the time-averaged off-surface quantities and time-dependent flowfields. Limited results and a brief discussion on Reynolds number effects are provided at the end. We conclude the paper with a short summary of key findings of the present study.

Computational Procedure

Flow Solver

The CFL3D code developed at LaRC has been used to compute the flowfield. Based on a finite-volume formulation, CFL3D solves the compressible form of three-dimensional, time-dependent, thin-layer Navier–Stokes equations. For the unsteady Reynolds averaged Navier–Stokes (URANS) computations, the two-equation shear stress transport (SST or k–ω) model of Menter [20] is used.

All current computations are performed using the second-order-accurate time discretization and the "dual time stepping" method [21]. Twenty-five subiterations, in conjunction with three-level W-type multigrid cycles, are used to ensure a minimum of 2 orders of magnitude drop in both the mean-flow and turbulence model residuals during each time step. To improve the convergence of the subiterations while maintaining stability, the pseudotime Courant–Friedrichs–Lewy (CFL) number was increased superlinearly from 1 to 10 within each time step. The subiteration procedure was deemed sufficiently converged when the lift and drag had plateaued.

Geometry and Grid Topology

The geometry under consideration is composed of two cylinders of equal diameter (D) aligned along the streamwise direction (tandem configuration) as shown in Fig. 1. The diameter of each cylinder is 1.75 in. (0.04445 m). The cylinders span the entire tunnel height b of 28 in. (0.71 m), yielding an aspect ratio of $b/D = 16$. Based on the tunnel width of 40 in. (1.016 m), the resulting model blockage (less than 4.4%) is deemed to be small enough to minimize the effects of tunnel wall interference. A more detailed account of the model hardware and its setup in BART is provided by JKCM. Of the three distinct separation distances (between the cylinders' centerline) of $L/D = 1.435$, 3.7, and 7.0 emphasized during the measurements by JKCM, only the cases of 1.435 and 3.7 are simulated numerically.

The global and near-field views of the grid topology for the $L/D = 3.7$ case are displayed in Fig. 2. Rather than simulating the actual test section in BART, the chosen computational domain is for a free-field flow to remove reflections of acoustic waves from the

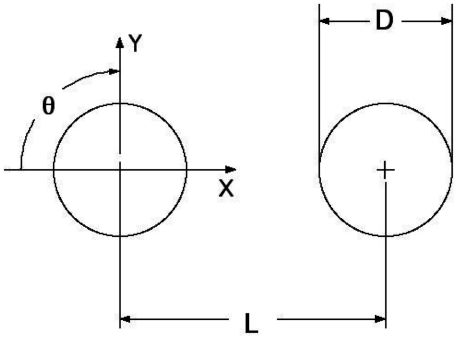

Fig. 1 Schematic diagram of simulated configuration.

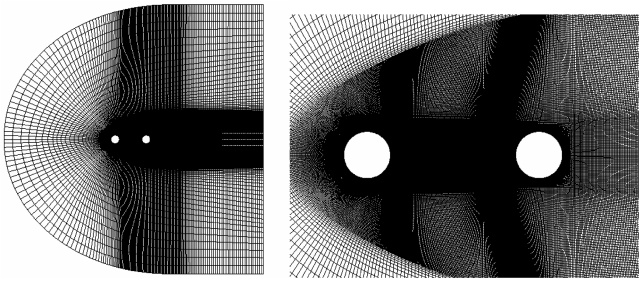

a) Full domain **b) Near-field grid**

Fig. 2 Computational domain and grid distribution ($L/D = 3.7$).

tunnel walls thereby facilitating the computation of far-field noise radiation in the future. The placement of the outer boundaries is a minimum of 13 diameters from the nearest point on the solid surfaces. Consistent with the objective behind this work, the computational grid is fine enough to resolve the dominant 2-D scales of motion in between the two cylinders and in the wake of the rear cylinder. However, as explained in the next section, there are regions of the flowfield that remain underresolved and, hence, may contribute to the observed discrepancies between the measurements and computations.

Originally, for the $L/D = 3.7$ case, the computational domain surrounding the cylinders was divided into 11 blocks, involving significant mesh clustering near the solid surfaces and in the cylinders' wakes. The structured and patched 2-D grid contained a total of 319 K grid points. Computations based on that grid were presented in [22]. After the initial set of computations, however, we found it beneficial to refine the original grid slightly. The present results are obtained with an improved grid that has 20 blocks and contains 401 K grid points. Within the immediate zone surrounding each cylinder, nearly 600 points are used along the circumferential direction and 150 points are packed in a radial distance of $0.2D$ in the wall normal direction.

Lessons learned from the $L/D = 3.7$ solutions were applied toward several subtle but important refinements of the grid for the $L/D = 1.435$ configuration. The most prominent refinement involved achieving better spatial resolution in the wake of the rear cylinder. For the $L/D = 1.435$ grid, the location of the outer boundaries remains identical to the previous case. The structured and patched 2-D grid contains a total of 316 K points distributed into 16 blocks.

The simulations were accomplished with a mix of runs that were executed on a single-processor machine as well as multiprocessor clusters. For the $L/D = 3.7$ case with 25 subiterations, it took 243 μs per cell per time step (or 96 s for the entire solution to be advanced one time step) on a 3.0 GHz Intel P4 Xeon based machine. Certainly, for a given grid, the computational cost varies directly with the number of subiterations needed to obtain a converged solution during time advancement.

Results

We now discuss the results of the numerical simulations normalized with respect to the cylinder diameter D, a reference speed U_∞, density, ρ_∞, and molecular viscosity, μ_∞. For the present study, the reference flow variables were set to match the conditions at the entrance to the BART test section. To simplify the emulation of the effect of boundary-layer trips on the front cylinder, the flowfield is assumed to be fully turbulent. The unsteady computations are based on the two-equation k–ω turbulence model [20]. The flow conditions for the simulations correspond to $M = 0.166$ and $Re = 1.66 \times 10^5$. However, limited additional results are also presented for higher Reynolds numbers. A constant nondimensional time step of $\Delta t = 0.00845$ (corresponding to 150 points per period for a 1000 Hz signal) is used throughout all simulations.

On the experimental side, velocities were measured using a 2-D, digital particle image velocimetry (DPIV) system. The system features two video cameras with a sensor size of 1360 pixels by 1024 pixels. The images from the two cameras were overlapped by 24 pixels to achieve an effective field of view approximately 156 mm wide and 60 mm high. A 1.5 mm thick light sheet was generated using a pulsed, frequency-doubled, 200 mJ neodymium-doped yttrium aluminium garnet (Nd-YAG) laser operated at 5 Hz and aligned to be perpendicular to the cylinder surfaces at a location 6 mm above the center pressure ring. A minimum of 1250 image pairs were acquired for each configuration and processed using the algorithm described in [23] with a 24 pixel by 24 pixel interrogation window and 50% overlap to obtain instantaneous velocities. The uncertainty in the PIV data is estimated to be ± 1.18 m/s.

As expected, simulations for the $L/D = 3.7$ case showed prominent vortex shedding from both cylinders. After the initial transient, the flowfield settled down into a quasi-periodic state with lift coefficients (root mean square) and shedding frequencies that were in line with available data [10,11,24] for high Reynolds number cylinder flows. The unsteady flow structures for the $L/D = 1.435$ configuration turned out to be less energetic and the fluctuation intensity was gradually damped out following the initial transient phase. We begin the discussion with time-averaged quantities for each of the two configurations, followed by a comparison of the instantaneous flowfields with the experiment.

Mean and RMS Surface Pressures

The time-averaged surface pressure coefficient Cp, for $L/D = 3.7$ is presented in Fig. 3. Distributions for both front and rear cylinders are displayed. As a partial measure of grid independence, results from the medium-level grid (where every other point in both directions was omitted from the finest grid) are also plotted on the figure. Notice that the mid- and fine-level Cps are nearly identical. Overall, the computed Cp displays a similar behavior to the measured pressure. The uncertainty in the pressure coefficient computed from the measured pressures is estimated to be ± 0.02. Both computation and measurement show a distribution that is

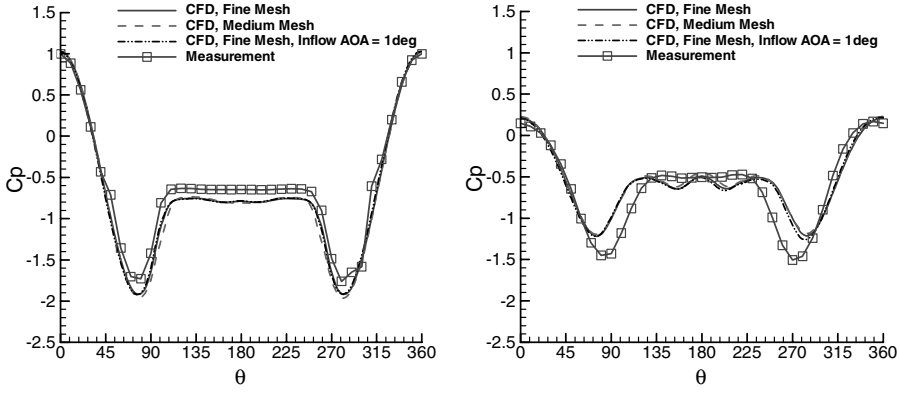

a) Front cylinder **b) Rear cylinder**

Fig. 3 Surface pressure distribution for $L/D = 3.7$, $M = 0.166$, and $Re = 1.66 \times 10^5$.

symmetric with two prominent suction peaks. The effect of the boundary-layer trips on the front cylinder (near $\theta = 50$ and $\theta = 310$ deg, respectively) is clearly visible in the form of slight irregularities in the measured Cp distribution. The computation overpredicts the magnitude of the suction peaks and has their location farther downstream on the front cylinder while underpredicting the magnitude of the pressure recovery toward the back portion of the cylinder. The dip in the pressure recovery near $\theta = 180$ deg has been observed in previous work related to a single cylinder [25], where it was attributed to the lack of three-dimensional effects within the computation. The computed separation points are located at $\theta = \pm 99$ deg on either side of the front stagnation point, indicating turbulent separation. The measured Cp shows an earlier separation for the tripped boundary layer by a few degrees, suggesting the presence of a wider wake than that being computed. In contrast to the front cylinder, the magnitude and location of the suction peaks are underpredicted for the rear cylinder, but good agreement is attained for the pressure recovery in the separated region. The computed separation points reside at $\theta = \pm 103$ deg while the measurements show delayed separation that is closer to 120 deg. The observed discrepancies between 315 and 360 deg may be due to a slight misalignment between the two cylinders.

The surface rms pressure distribution on both cylinders is plotted in Fig. 4. The results based on the medium mesh solution are also displayed as a more stringent grid convergence indicator. The relatively good agreement obtained highlights the adequacy of our fine mesh solution to capture the pertinent features of the flow field. Measurements by JKCM did not include unsteady surface pressures; hence the results in Fig. 4 cannot be compared with data at the present time. An additional curve included in Fig. 4 corresponds to the computed surface pressure fluctuations when the incoming flow is at 1 deg relative to the line of symmetry of the cylinder configuration. We will return to that result in a later section when we discuss the effects of flow asymmetry in tunnel flow. Returning to Fig. 4, the computed rms pressure distribution on the front cylinder has a single dominant peak. As would be suspected, the fluctuations attain their highest level at or near the point of separation. For the present computations, the peaks reside at $\theta = \pm 94$ deg that is slightly ahead of the separation locations. The rapid variation and the magnitude of drop in rms levels near $\theta = 180$ deg is an anomaly that could not be blamed on the lack of resolution but rather may be attributed to the lack of three-dimensional effects or inadequacies of the turbulence model. Except for near the base region, the present rms pressure profile and the associated peak location are in good agreement with the measurements of Sun et al. [12] that were obtained at a supercritical $Re = 6.5 \times 10^5$. On the other hand, the computed rms pressures show much higher levels compared to their measurements which we believe could be attributed to the differences in the Reynolds number. In fact, the present levels are in better agreement with subcritical Reynolds number measurements of Igrashi [4] and Arie et al. [11] where the Reynolds numbers are closer to the present value.

In agreement with the available measurements [4,11,12], the rear cylinder exhibits higher fluctuation levels (Fig. 4b) relative to the front cylinder. The rms profile depicts a dual peak structure. The prominent peak, situated close to $\theta = 40$ deg, is the result of shed vortices from the front cylinder impacting the rear cylinder surface. The less prominent peak ($\theta = 98$ deg), as in the case of the front cylinder, occurs in the vicinity of the point where the boundary layer separates. A point worth noting here is that for sufficiently large Reynolds numbers, due to the incoming turbulent wake, the rear cylinder always experiences a turbulent boundary layer and separation. As such, the primary differentiating factor between various measurements should be the actual value of the Reynolds

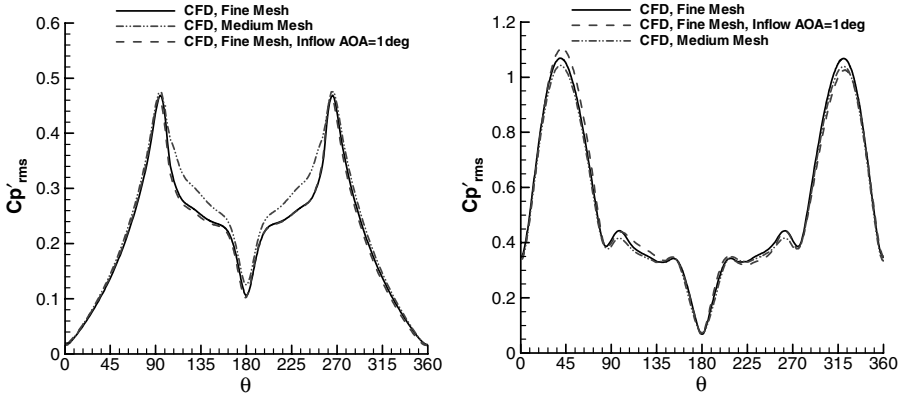

a) Front cylinder **b) Rear cylinder**

Fig. 4 Surface rms pressure distribution for $L/D = 3.7$, $M = 0.166$, and $Re = 1.66 \times 10^5$.

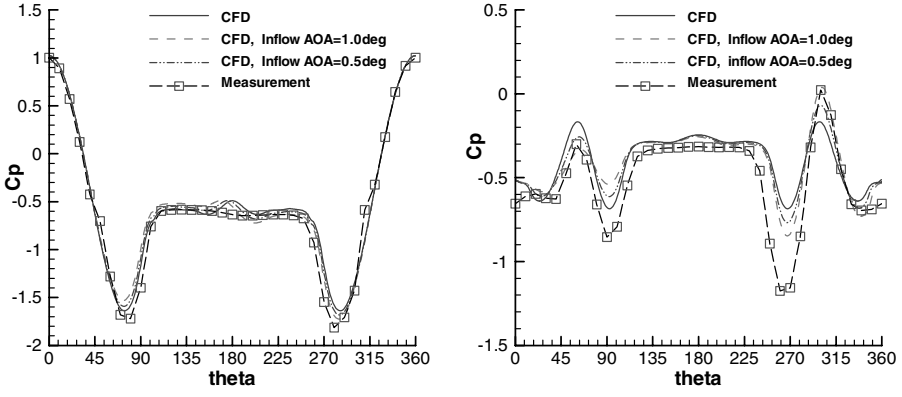

a) Front cylinder **b) Rear cylinder**

Fig. 5 Surface pressure distribution for $L/D = 1.435$, $M = 0.166$, and $Re = 1.66 \times 10^5$.

number at which the experiment was executed. This would explain why the computed rms pressure levels and profile are in better agreement with the subcritical Reynolds number measurements of [4,11] rather than those of [12] which were conducted at a supercritical Reynolds number. We will return to this issue in a later section.

The Cp results for the case of $L/D = 1.435$ are plotted in Fig. 5. For the initial comparison, focus on the two curves labeled "CFD" (solid line) and "Measurement" (line with symbols). For the front cylinder (Fig. 5a), the computed pressures are in good agreement with the measurement. The magnitude and locations of the suction peaks and the separation points are well predicted as is the magnitude of the pressure recovery in the back. In contrast to both single cylinder and tandem configurations with larger separations, the computational fluid dynamics (CFD) result moderately overpredicts the base pressure behind the front cylinder at $L/D = 1.435$. The reason for this overprediction is not clear at this stage. Notice that there is a slight asymmetry to the measured Cp. For the rear cylinder (Fig. 5b), the high-pressure peak does not occur along the $\theta = 0$ line. Two separate high-pressure peaks are observed at $\theta \approx \pm 50$ deg, close to where the shear layers separating from the front cylinder impinge on the rear cylinder. The computed pressure shows the relevant trends but does not predict the measured amplitudes for these peaks. Most significantly, the mean CFD-based pressures are nominally symmetric about $\theta = 0$, whereas a pronounced asymmetry is noted in the measured Cp distribution along the surface of the rear cylinder. As alluded to above, such a strong pressure asymmetry on the rear cylinder has also been observed by previous investigators [6,14], but we are unaware of any clear explanation for its occurrence.

During the course of the experiments by JKCM, particular care was exercised to ensure nearly symmetric pressure distributions along both the front and the rear cylinders. Although for larger separation distances it was relatively easy to achieve a near symmetric Cp distribution, the pressure field became extremely sensitive to even minor perturbations for L/D less than 1.5. On certain occasions, it was possible to achieve close to symmetric pressure distributions, while routine (and seemingly minor) changes during the course of the testing phase resulted in a loss of symmetry at small separation distances. During the postexperiment discussions, the possibility that the presence of small irregularities whether in the misalignments of the fabricated model, model setup in the tunnel, or incoming flow angularities could cause the asymmetry was raised. In particular, the effects of incoming flow angularity were deemed to be most critical because ultimately geometrical misalignments [6] would also manifest themselves as a change in the incoming flow direction. It was further conjectured that minor incoming flow angularities would have less of an impact once the separation distance between the two cylinders is large enough to allow fully established shedding from each cylinder. To test these hypotheses, a series of 2-D simulations were carried out whereby the approaching inflow was at a nonzero but small angle of attack (AOA). Going back

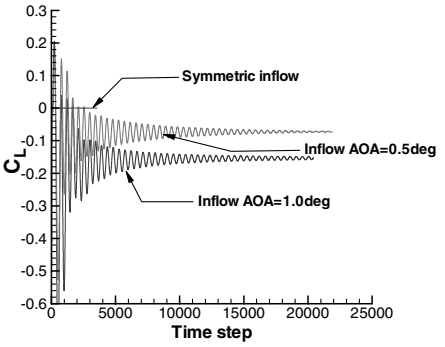

Fig. 6 Effect of incoming flow angularity on total lift for $L/D = 1.435$.

to Fig. 3, notice that an AOA of 1 deg has hardly any influence on the predicted surface pressure distribution at $L/D = 3.7$. In contrast, for the $L/D = 1.435$ case, even a small change in the incoming flow direction produces large surface pressure asymmetries on the rear cylinder that are in line with the measured trends. Figure 6 shows the effect of inflow angularity on the total lift coefficient C_L. Observe that imparting a vertical velocity that is less than 2% of the freestream velocity results in a mean lift coefficient of approximately -0.16. A more challenging question is whether and how such small imperfections can be eliminated from an experimental setup and what impact that would have on the observed asymmetry. Surely, whether documented or not, most entrance flows to any tunnel test section involve a small amount of flow angularity. Similar asymmetry also occurs naturally in complex flow configurations such as an aircraft undercarriage.

Time-Averaged Off-Surface Quantities

The mean streamlines for the $L/D = 3.7$ are shown in Fig. 7. The experimental streamlines are obtained from averaging over 1000 PIV snapshots. The plots provide useful insight into the extent of flow separation behind each cylinder. In contrast to the measurements, the computations predict that the larger of the two (mean) separation zones occurs behind the rear cylinder. One possible reason for this difference could be a lack of both sufficiently strong unsteady flow structures and 3-D effects in the computation. In the experiment, fluid trapped within the recirculating zone can get pumped out by the weak spanwise flow along the base of the cylinder. Certainly, such effects are not captured by our 2-D simulations. As expected from the examination of the Cp plots, the computation shows a narrower wake and thus a shorter recirculation zone for the front cylinder. However, the observed differences for the separation zone of the front cylinder are somewhat more difficult to explain. In addition to the absence of 3-D effects, other possible reasons may involve the turbulence model's effects or a lack of accounting for the boundary-layer trip effects in our experiment. Also note a slight asymmetry in

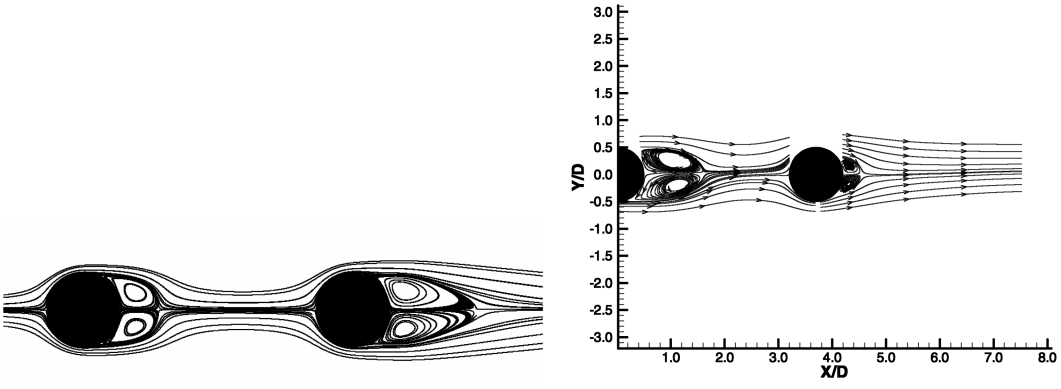

a) Computation **b) Experiment**

Fig. 7 Mean streamlines for $L/D = 3.7$.

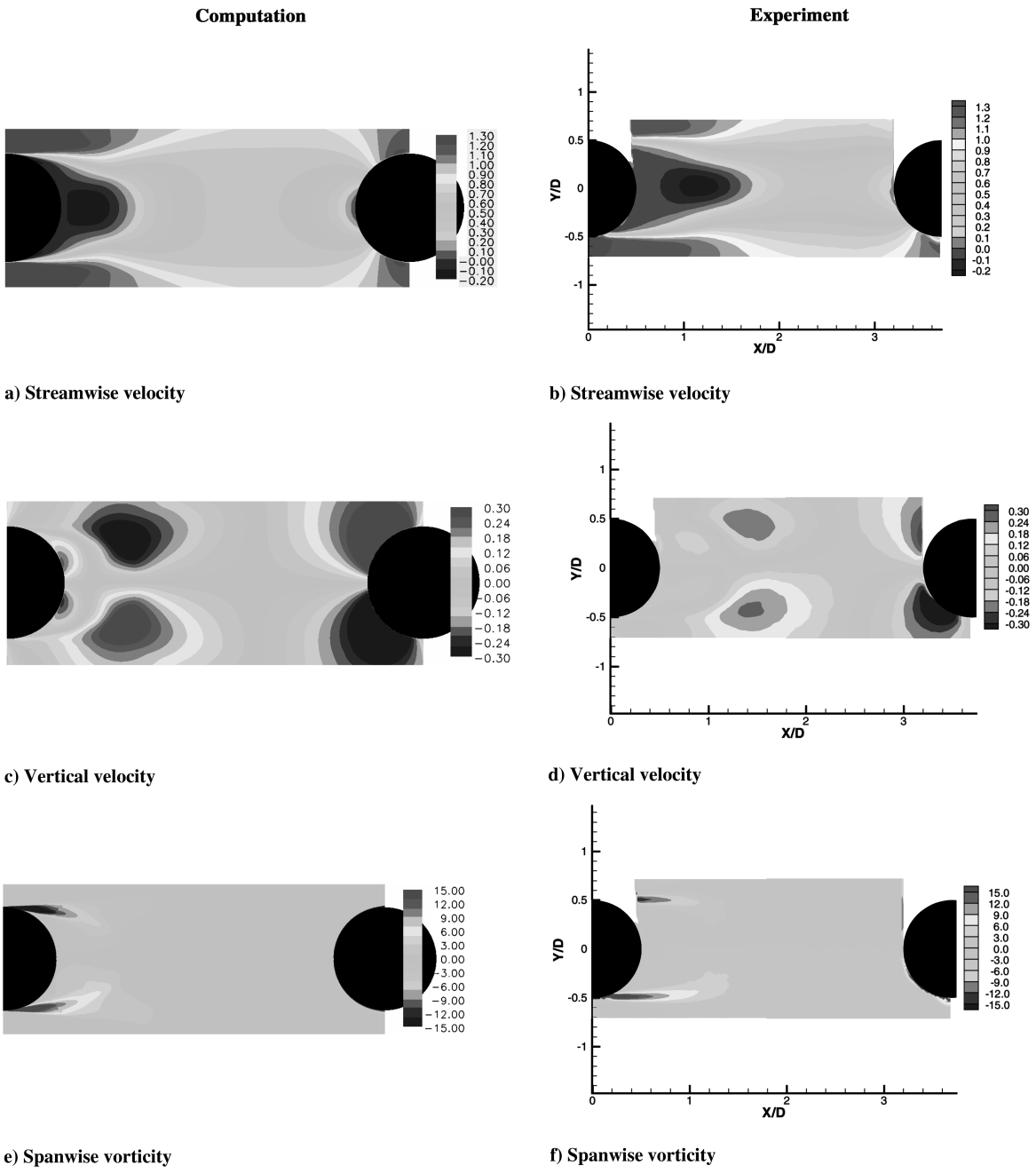

Fig. 8 Mean velocity and vorticity fields for $L/D = 3.7$, $M = 0.166$, and $Re = 1.66 \times 10^5$.

the measured streamlines between the cylinders, pointing to the possibility of a small flow angularity as discussed earlier.

The corresponding averaged streamwise and vertical velocity contours plus the spanwise vorticity field for the region in between the two cylinders are plotted in Fig. 8. As expected, the computed velocity contours show a shorter recirculation zone compared with PIV data, along with a more rapid recovery in the wake deficit within the gap region. The slower recovery in the measured wake results in mean velocities in the region ahead of the rear cylinder that are on the order of 20 to 30% of U_∞. The computed vertical velocities show the proper trends but tend to be larger than measured values, suggesting an artificially prominent roll-up (shedding) process in the URANS solution. The computed vorticity contours diffuse very rapidly at much closer distances to the solid surface than indicated by the measurements. To adequately capture the evolution of the curved shear layer at such distances from the cylinder surface will require a much higher spatial resolution than that of the present computations.

For aeroacoustic modeling purposes, an in-depth knowledge of the fluctuating flowfield is of paramount importance. The rms velocity fluctuations and the corresponding turbulent kinetic energy (TKE) plots for $L/D = 3.7$ are displayed in Fig. 9. Although the overall patterns are captured correctly, the computations tend to overpredict the magnitude of the perturbations. There could be several explanations for this overprediction, starting with the 2-D nature of our simulations along with intrinsic limitations of using conventional turbulence models for time-accurate CFD. The second explanation involves the fact that the vortex shedding process in the simulations is a single-frequency (i.e., artificially regular) event that tends to be more intense compared with the actual vortex roll-up and shedding processes. The latter (as will be seen in the next section) are much more diffuse, involving interactions among a variety of scales.

The mean streamline patterns for $L/D = 1.435$ are shown in Fig. 10. Given the above discussion on the Cp asymmetry in the measured data, only simulated results obtained at AOA $= 1.0$ deg will be used for the remainder of the paper. For this case, the

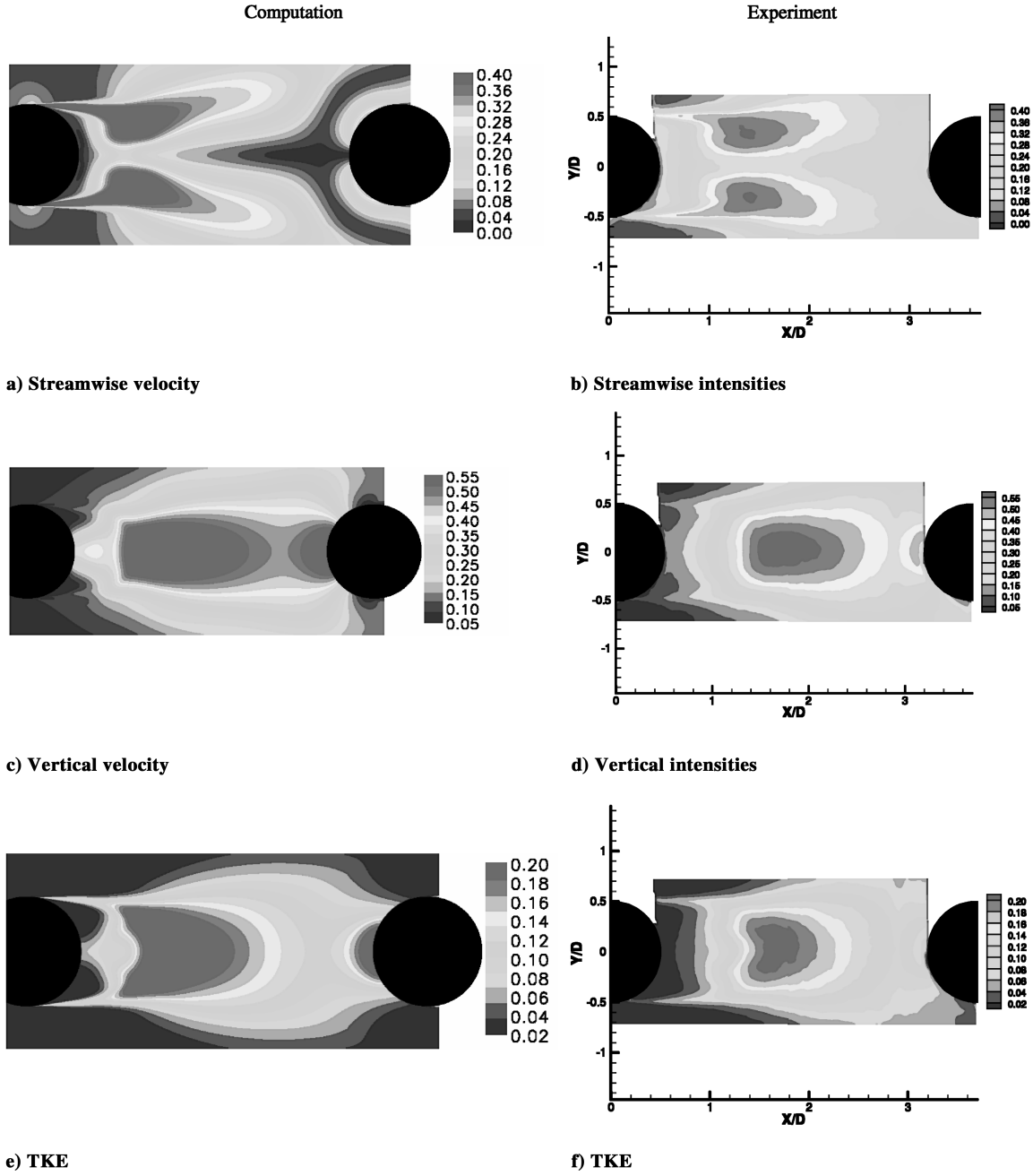

Fig. 9 Mean fluctuating field for $L/D = 3.7$, $M = 0.166$, and $Re = 1.66 \times 10^5$.

computed length ($\approx 1.4D$) of the separation zone behind the rear cylinder agrees better with the measurement than the 3.7 case does. Notice that the computed streamlines are asymmetric, showing a dual structure pattern within the gap region with a larger cell on the bottom. Similar gap-flow asymmetry was captured by the PIV measurements of Lin et al. [9] conducted at $Re = 1.0 \times 10^4$. In contrast, the current measured streamlines show a single large recirculating zone with fluid particles moving in the counter-clockwise direction. The existence of a much smaller second cell within the gap may have been lost due to insufficient resolution of the PIV setup or other postprocessing deficiencies. Most likely, the asymmetric gap pattern in the experiment is established by a combination of incoming flow angularity and a nonzero spanwise flow toward the tunnel's ceiling and floor. For the 2-D simulations, however, once the detached shear layers from the front cylinder reattach to the rear cylinder, the fluid particles within the gap zone are trapped without the possibility of escaping the zone.

Contour plots of the mean velocities and the spanwise vorticity for $L/D = 1.435$ at AOA $= 1.0$ deg are presented in Fig. 11 and show reasonable agreement between the predicted and measured data. Also observe that the direction of the computed mean vertical velocity (Fig. 11c) within the gap region is opposite to that observed for the $L/D = 3.7$ configuration (Fig. 8c). Although reversal of the velocity direction is understandable (due to the presence of the dual recirculating structures), the magnitudes of the peak velocities are a bit surprising. According to the literature, a reduced gap should result in progressively more stagnated flow within this zone. Notice that the measurements also show comparable velocity magnitudes within the gap albeit a different flow structure. But, as discussed in JKCM, the gap region possesses a relatively weak perturbation field and, therefore, may not be aeroacoustically significant. The spanwise vorticity field (Fig. 11e) clearly displays the formation of the free-shear layers and their detachment locations from the front cylinder. The computed shear layers reattach to the rear cylinder without going through a typical roll-up process, reinforcing the notion that the tandem cylinders act as a single bluff body for short gaps. As alluded to in earlier sections, after the initial transient state, the $L/D = 1.435$ computations revealed a decaying time-dependent flowfield (Fig. 6)

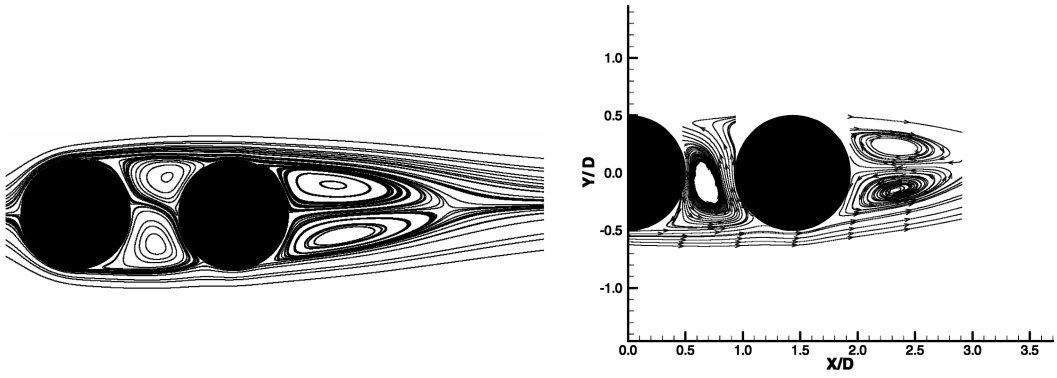

a) Computation **b) Experiment**

Fig. 10 Mean streamlines for $L/D = 1.435$, AOA = 1 deg.

with rapidly diminishing fluctuating fields. This premature decay of the fluctuations is reminiscent of our previous time-accurate simulations for high-lift wings [26,27]. In those instances, the SST (k–ω) turbulence model proved to be excessively diffusive thus damping weaker flow unsteadiness. It suffices to say that the PIV and hot-wire measurements (see JKCM) all indicate the fluctuating fields to be much less energetic than the corresponding fields for $L/D = 3.7$. It is therefore plausible that the excessive diffusiveness of the turbulence model has had similar damping effects on the weaker fluctuating field encountered at the smaller spacing. Although not shown here, we have repeated the simulation for $L/D = 1.435$, using the Spalart–Allmaras turbulence model [28]. The end result was the same, suggesting that the lack of maintenance of flow fluctuations is not unique to the SST model employed in current simulations.

Time-Dependent Flowfield

A sample plot of the instantaneous spanwise vorticity field from the $L/D = 3.7$ simulation is shown in Fig. 12. Important features such as boundary-layer separation, shear-layer formation, roll-up, and the formation of discrete vortices are clearly depicted in this figure. The vorticity field shows the convection and interaction of the vortices with the rear cylinder. The stagnation point on the front of the rear cylinder exhibits large excursions about the zero degree line due to this interaction. Also note the large undulation of the shear layers emanating from the rear cylinder before the roll-up process takes place. As indicated earlier, the simulated shedding process shows an intense event whereby the detached vorticity rolls up into large-scale vortices scaling with the cylinder diameter. In contrast, the PIV snapshot in Fig. 12b shows a more scattered roll-up process that is composed of a large number of structures with a smaller scale. Additional noteworthy features of the PIV snapshot include the presence of smaller rollers residing within the detached shear layer and the amalgamation of these rollers into a large structure that resembles a typical shed vortex. Note that the smaller rollers maintain their individual identity even up to the time they reach the rear cylinder. The smaller vorticity lumps in Fig. 12b are the result of KH instabilities in the free shear layer, which represent the local, large-scale motion of the flow and are known to scale with the shear-layer thickness. The presence of KH instabilities in a cylinder wake was first observed by Couregelongue [29] as early as 1929. Figure 13a, reproduced from Zdravkovich [24], shows a schematic depiction of wake structures based on Couregelongue's observation of the flowfield at $1.2 \times 10^3 < Re < 1.0 \times 10^4$. The smaller vortices riding on the mixing layers were called "transition eddies" by these investigators. A sample of our PIV snapshot that depicts similar flow topology is also shown in Fig. 13b. In their PIV study of tandem cylinders at $Re = 1.0 \times 10^4$, Lin et al. [9] also observed KH instabilities and the accompanying convective rollers. The measurements by JKCM at $Re = 1.66 \times 10^5$ indicate that the dynamics of KH instabilities and their effects on the wake structure can be observed over a large range of Reynolds numbers. The PIV data of JKCM showed the growth of KH instabilities for $L/D = 1.435$ (analogous to the $L/D = 3.7$ case) and the resulting chain of vortices that are convected downstream.

JKCM used hot-wire measurements to obtain frequency spectra of velocity fluctuations for both $L/D = 3.7$ and $L/D = 1.435$. The measured spectra at a location $2.7D$ downstream and $0.69D$ below the axis of the rear cylinder are shown in Fig. 14. For reference, the figure includes the hot-wire spectrum for the single cylinder case at the same location relative to the cylinder axis. The peak frequency and the corresponding Strouhal number St are also indicated for each curve. The spectrum for $L/D = 3.7$ possesses a distinct narrowband peak that is an order of magnitude above the surrounding frequencies. The spectrum for $L/D = 1.435$ displays a significantly lower but broader peak that contains approximately 60% of the energy compared with the peak at $L/D = 3.7$ (or, equivalently, 39% of the energy contained within the peak for the single cylinder case). It is not clear how or if this change in the character of the Strouhal shedding is related to the previously discussed absence of self-sustaining, unsteady structures within the CFD simulations.

A sample time history of the computed lift (C_L) and drag (C_D) coefficients for $L/D = 3.7$ is shown in Fig. 15. For clarity, only the last 2000 time steps of the computation are plotted. Notice C_L and C_D are periodic with a shedding frequency of approximately 299 Hz ($St = 0.237$) for both front and rear cylinders. This value is close to the measured frequency of 303 Hz ($St = 0.24$), although one must bear in mind that the hot-wire spectrum is based on local velocity fluctuations at a single point. The fact that both cylinders have the same shedding frequency is in agreement with Okajima's [10] hot-wire measurements at transcritical Reynolds numbers. However, his measurements show the Strouhal number to be different depending on the form of surface roughness on the front cylinder ($St = 0.26$–0.27 for localized roughness and $St = 0.2$ for full roughness). From Fig. 15a, note the rear cylinder experiences larger lift oscillations that are nearly 130 deg out of phase with those associated with the front cylinder. Similar behavior is observed from the C_D plots in Fig. 15b, corroborating the measurements of Arie et al. [11]. The time-averaged drag coefficient is 0.71 for the front and 0.32 for the rear cylinder, respectively. Both values are in close agreement with Okajima's [10] measurements when the front cylinder was tripped. The predicted lift coefficient for the $L/D = 1.435$ case maintains a weak periodic state while the oscillations are being damped in time, as seen from Fig. 6. The frequency of these oscillations is close to 310 Hz ($St = 0.246$), which is 12% lower than the measured value of 353 Hz ($St = 0.28$).

Reynolds Number Effects

An important issue when it comes to cylinder flow is the effects of the Reynolds number on the state of the wake. We repeated the $L/D = 3.7$ simulation for $Re = 6.0 \times 10^5$ and 1.0×10^6 while keeping the Mach number constant. Given the excellent agreement

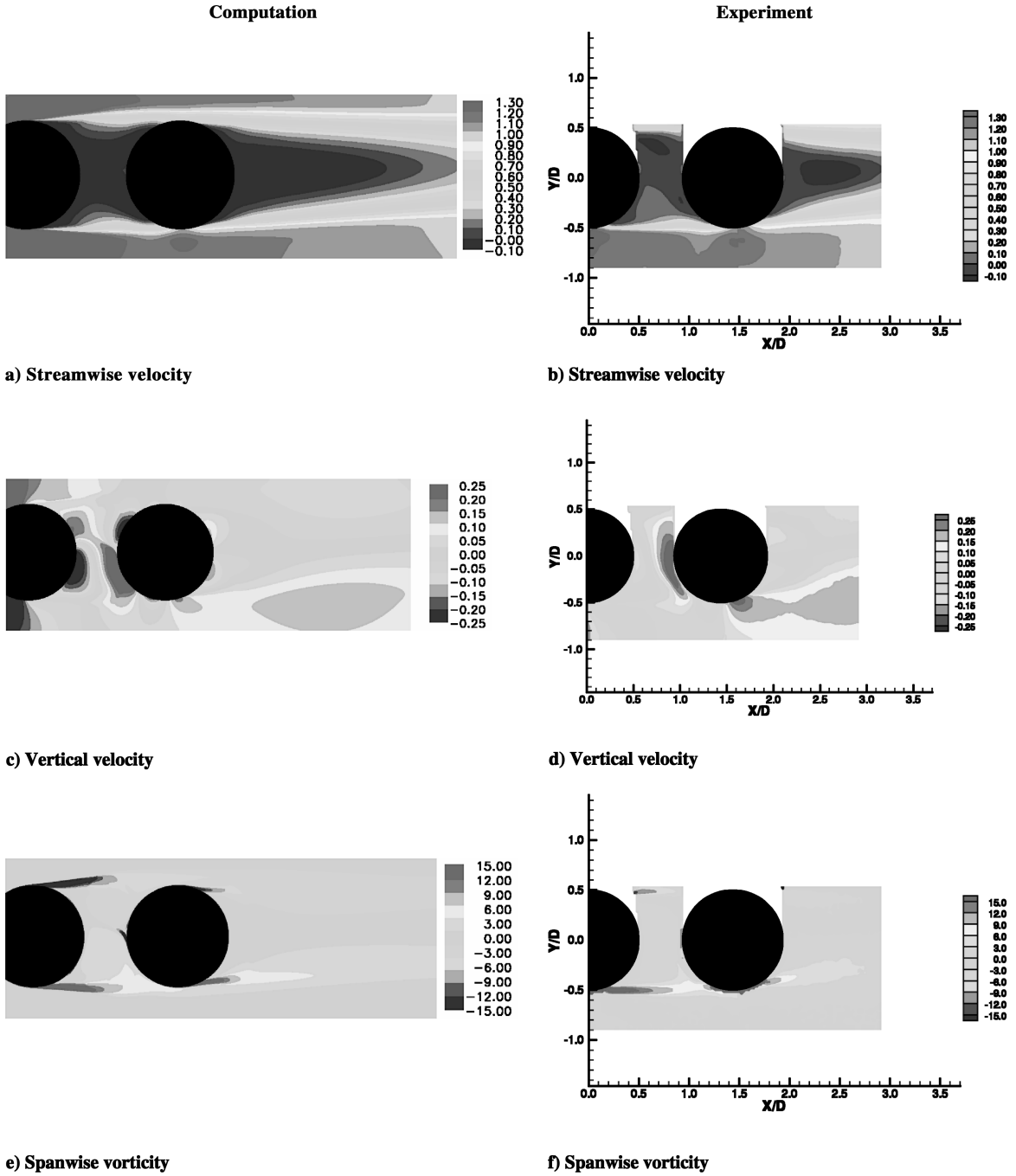

a) Streamwise velocity

b) Streamwise velocity

c) Vertical velocity

d) Vertical velocity

e) Spanwise vorticity

f) Spanwise vorticity

Fig. 11 Mean velocity and vorticity fields for $L/D = 1.435$, $M = 0.166$, and $Re = 1.66 \times 10^5$.

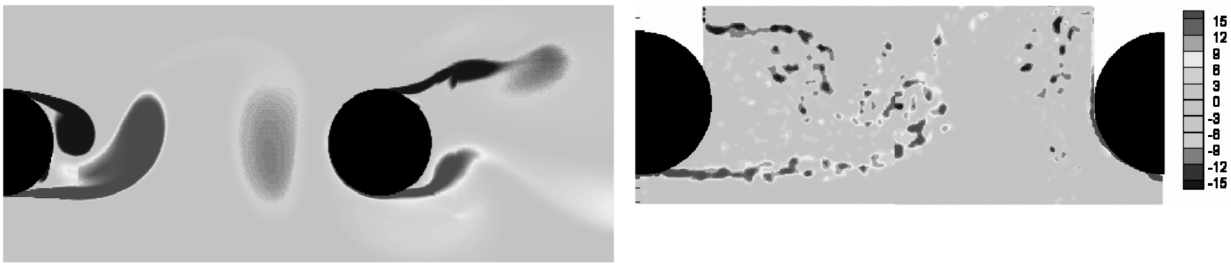

a) Computation

b) Experiment

Fig. 12 Instantaneous spanwise vorticity field for $L/D = 3.7$.

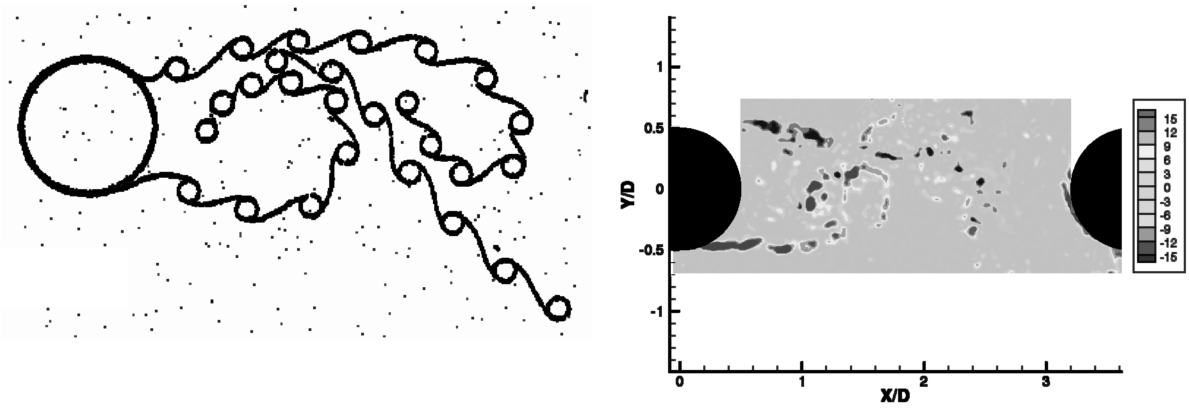

a) b)

Fig. 13 Schematic of wake structures as observed by Couregelongue a) and a PIV snapshot of instantaneous vorticity field b) showing similar structures.

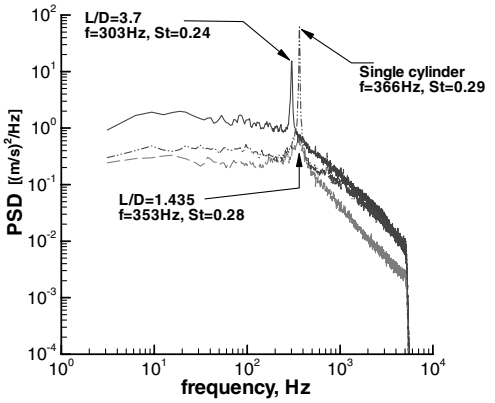

Fig. 14 Velocity fluctuation spectrum indicating shedding frequency, measured by hot wire at a downstream streamwise distance of approximately 2.7 diameters and $Y/D = -0.69$ behind the rear cylinder or single cylinder. PSD stand for power spectral density.

between our medium-grid and fine-grid solutions at $Re = 1.66 \times 10^5$, it was decided that the fine grid might also be adequate for unsteady calculations at the higher Reynolds numbers. The predicted surface Cp distributions at the higher Reynolds number plus the measured Cp at $Re = 1.66 \times 10^5$ are plotted in Fig. 16. On the front cylinder, the higher Reynolds number tends to improve the pressure recovery along the leeward side, but slightly worsens the windward suction peaks. The Cp distribution for the rear cylinder shows significantly improved agreement with the measured pressures. The magnitude and location of the suction peaks as well as the base pressure recovery are consistent with measurements. Root-mean-square surface pressure distributions are displayed in Fig. 17. The figure clearly shows that increasing the Reynolds number lowers surface pressure fluctuations. In particular, the levels for the front cylinder show a significant drop in rms amplitude over the entire surface. At these super- and transcritical Reynolds numbers, the computed rms pressure distributions for the front cylinder are in good agreement with the measurements of Sun et al. [12] conducted at $Re = 6.5 \times 10^5$ and lends support to their observation that interference effects (measured by the magnitude of the primary rms peak on the rear cylinder) become weaker as the Reynolds number is increased from subcritical to supercritical levels. Because of space limitations, comparison between the PIV measurements and the postprocessed high-Reynolds number results will be limited to the presentation of the TKE field shown in Fig. 18. It is evident from Fig. 18 that the computed turbulent kinetic energy compares well with the measured field (Fig. 9f). It suffices to say, we have scrutinized the computed flowfields, and, in every aspect, they show noticeably better agreement with the measured data that are presented in Figs. 8 and 9 than those results obtained at $Re = 1.66 \times 10^5$. Obviously, the computed Reynolds number trends point to the fact that the effects of the boundary-layer trip on the front cylinder are far more complex than can be duplicated by the mere application of a fully turbulent flow in the computations. In the simulations, the boundary-layer transition from a laminar to a turbulent state is determined by the turbulence model. Certainly, one could employ an equivalent Reynolds number (that would account for the tripping effects) for performing the computations. However, we are not aware of any straightforward criteria to determine such value for the Reynolds number.

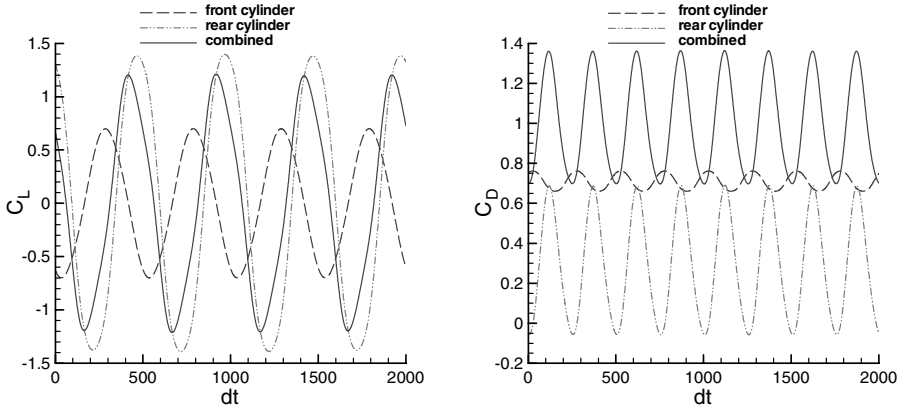

a) Front cylinder b) Rear cylinder

Fig. 15 Time variation of lift and drag coefficients for $L/D = 3.7$, $M = 0.166$, and $Re = 1.66 \times 10^5$.

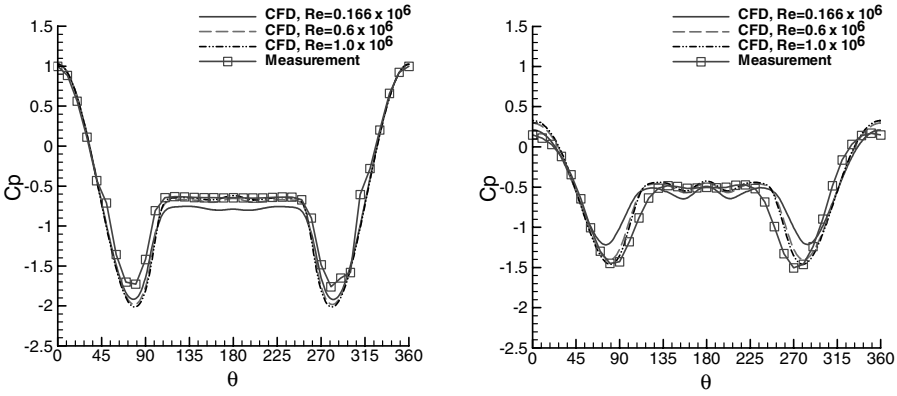

a) Front cylinder b) Rear cylinder

Fig. 16 Reynolds number effects on surface pressure distribution for $L/D = 3.7$, $M = 0.166$.

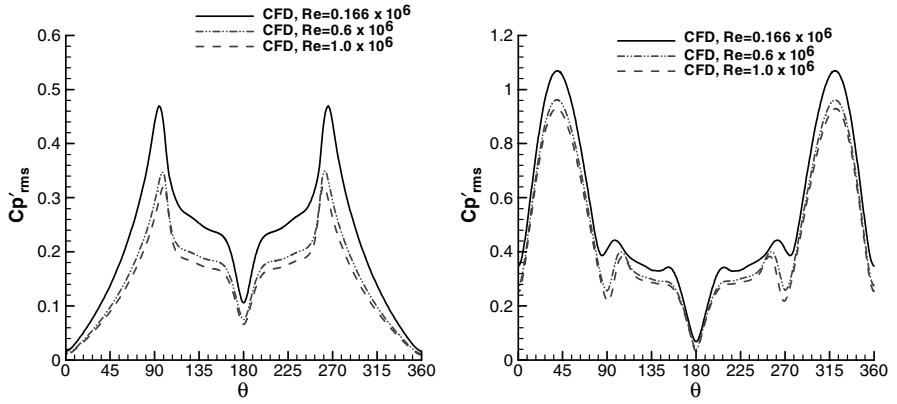

a) Front cylinder b) Rear cylinder

Fig. 17 Reynolds number effects on surface rms pressure distribution for $L/D = 3.7$, and $M = 0.166$.

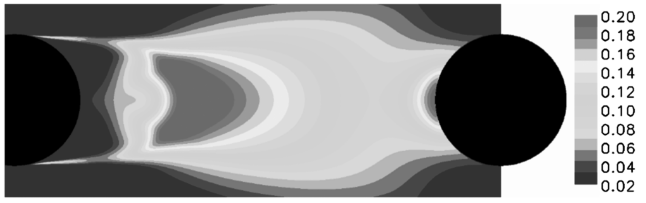

Fig. 18 Mean TKE field for $L/D = 3.7$, $M = 0.166$, and $Re = 1.0 \times 10^6$.

Conclusions

A combined computational and experimental effort is directed toward understanding highly interactive flow fields between multiple bluff bodies that are representative of flows encountered in main landing gears. A pair of cylinders in tandem configuration is a canonical geometry that occurs often in main gears. The computations are focused on 2-D simulations of the flow past a tandem configuration for separation distances of $L/D = 1.435$ and 3.7, representing small and medium gaps, respectively. For $L/D = 3.7$, vortex shedding occurs on both cylinders, and a periodic global state is established within the URANS computations. The computed shedding frequency based on the oscillations in the individual cylinder lift is 299 Hz, which agrees quite well with the experimentally measured frequency of 303 Hz. The character of the flowfield changes dramatically when the gap is reduced to 1.435. The shear layers detaching from the front cylinder reattach to the rear cylinder surface, effectively creating a single bluff body. However, for $L/D = 1.435$, the computations are unable to sustain the initial flow unsteadiness. Thus, the fluctuating field gets damped over time. Whether or not the predicted weakness of fluctuations at $L/D = 1.435$ is related to the diffuse nature of the Strouhal peak in the measured hot-wire spectrum remains to be determined. The sensitivity of the CFD solution to slight changes in the angle of attack at short separation distances may explain the occurrence of asymmetric mean flows in previous experiments.

Instantaneous vorticity fields based on the PIV measurements indicate highly dynamic wakes at both short and intermediate separation gaps. PIV data also reveal the prominence of smaller scale vortex structures that arise as Kelvin–Helmholtz instabilities within shear-layer regions. The current URANS computations are incapable of capturing the full wake dynamics as observed in the PIV snapshots.

Acknowledgment

The authors would like to express their appreciation to M. R. Wiese of the Analytical Services and Materials, Inc., for generating the grids used in the computations.

References

[1] Zdravkovich, M. M., "Review of Flow Interference Between Two Circular Cylinders in Various Arrangements," *Journal of Fluids Engineering*, Vol. 99, Dec. 1977, pp. 618–633.

[2] Ohya, Y., Okajima, A., and Hayashi, M., "Wake Interference and Vortex Shedding," *Encyclopedia of Fluid Mechanics*, edited by N. P.

Cheremisinoff, Vol. 8, Gulf Publishing Company, Houston, TX, 1989, pp. 323–389.
[3] Zdravkovich, M. M., "Flow Induced Oscillations of Two Interfering Circular Cylinders," *Journal of Sound and Vibrations*, Vol. 101, No. 4, 1985, pp. 511–521.
[4] Igarashi, T., "Characteristics of the Flow Around Two Circular Cylinders Arranged in Tandem (1st Report)," *Bulletin of the JSME*, Vol. 24, No. 188, Feb. 1981, pp. 323–331.
[5] Igarashi, T., "Characteristics of the Flow Around Two Circular Cylinders Arranged in Tandem (2nd Report, Unique Phenomena at Small Spacing)," *Bulletin of the JSME*, Vol. 27, No. 233, Nov. 1984, pp. 2380–2387.
[6] Ljungkrona, L., Norberg, C. H., and Sunden, B., "Free-Stream Turbulence and Tube Spacing Effects on Surface Pressure Fluctuations for Two Tubes in an In-Line Arrangement," *Journal of Fluid and Structures*, Vol. 5, No. 6, 1991, pp. 701–727.
[7] Ljungkrona, L., and Sunden, B., "Flow Visualization and Surface Pressure Measurement on Two Tubes in an Inline Arrangement," *Experimental Thermal and Fluid Science*, Vol. 6, No. 1, 1993, pp. 15–27.
[8] Wu, J., Welch, L. W., Welsh, M. C., Sheriden, J., and Walker, G. J., "Spanwise Wake Structures of a Circular Cylinder and Two Circular Cylinders in Tandem," *Experimental Thermal and Fluid Science*, Vol. 9, No. 3, 1994, pp. 299–308.
[9] Lin, J.-C., Yang, Y., and Rockwell, D., "Flow Past Two Cylinders in Tandem: Instantaneous and Averaged Flow Structure," *Journal of Fluid and Structures*, Vol. 16, No. 8, Dec. 2002, pp. 1059–1071.
[10] Okajima, A., "Flows Around Two Tandem Circular Cylinders at Very High Reynolds Numbers," *Bulletin of the JSME*, Vol. 22, No. 166, April 1979, pp. 504–511.
[11] Arie, M., Kiya, M., Moriya, M., and Mori, H., "Pressure Fluctuations on the Surface of Two Circular Cylinders in Tandem Arrangement," *Journal of Fluids Engineering*, Vol. 105, June 1983, pp. 161–167.
[12] Sun, T. F., Gu, Z. F., He, D. X., and Zhang, L. L., "Fluctuating Pressure on Two Circular Cylinders at High Reynolds Numbers," *Journal of Wind Engineering and Industrial Aerodynamics*, Vols. 41–44, Nos. 1–3, 1992, pp. 577–588.
[13] Gu, Z. F., Sun, T. F., He, D. X., and Zhang, L. L., "Two Circular Cylinders in High-Turbulence Flow at Supercritical Reynolds Number," *Journal of Wind Engineering and Industrial Aerodynamics*, Vol. 49, Nos. 1–3, 1993, pp. 379–388.
[14] Gu, Z. F., "On Interference Between Two Circular Cylinders at Supercritical Reynolds Number," *Journal of Wind Engineering and Industrial Aerodynamics*, Vol. 62, Nos. 2–3, 1996, pp. 175–190.
[15] Gu, Z. F., and Sun, T. F., "On Interference Between Two Circular Cylinders in Staggered Arrangement at High Subcritical Reynolds Numbers," *Journal of Wind Engineering and Industrial Aerodynamics*, Vol. 80, No. 3, 1999, pp. 287–309.
[16] Sun, J., Li, J., and Roux, B., "Flow Regimes and Frequency Selection of a Cylinder Oscillating in an Upstream Cylinder Wake," *International Journal for Numerical Methods in Fluids*, Vol. 16, No. 10, 1993, pp. 915–929.
[17] Mittal, S., Kumar, V., and Raghuvanshi, A., "Unsteady Incompressible Flows Past Two Cylinders in Tandem and Staggered Arrangements," *International Journal for Numerical Methods in Fluids*, Vol. 25, No. 11, 1997, pp. 1315–1344.
[18] Itoh, Y., and Himeno, R., "Numerical Simulation of Three-Dimensional Flow Around Two Circular Cylinders in Tandem Arrangement," RIKEN Review No. 48: Focused on High Performance Computing in RIKEN 2001, Oct. 2002, pp. 3–6.
[19] Jenkins, L. N., Khorrami, M. R., Choudhari, M. M., and McGinley, C. B., "Characterization of Unsteady Flow Structures Around Tandem Cylinders for Component Interaction Studies in Airframe Noise," AIAA Paper AIAA-2005-2812, May 2005.
[20] Menter, F., "Improved Two-Equation k-ω Turbulence Models for Aerodynamic Flows," NASA TM 103975, 1992.
[21] Rumsey, C. L., Sanetrik, M. D., Biedron, R. T., Melson, N. D., and Parlette, E. B., "Efficiency and Accuracy of Time-Accurate Turbulent Navier-Stokes Computations," *Computers and Fluids*, Vol. 25, No. 2, 1996, pp. 217–236.
[22] Khorrami, M. R., Choudhari, M. M., Jenkins, L. N., and McGinley, C. B., "Unsteady Flowfield Around Tandem Cylinders as Prototype for Component Interaction in Airframe Noise," AIAA Paper 2005-2866, May 2005.
[23] Lourenco, L. M., and Krothapalli, A., "True Resolution PIV: A Mesh-Free Second Order Accurate Algorithm," *Proceedings of the 10th International Symposium on Applications of Laser Techniques to Fluid Mechanics*, Organizing Committee of the 10th International Symposium on Applications of Laser Techniques to Fluid Mechanics, Lisbon, July 2000.
[24] Zdravkovich, M. M., *Flow Around Circular Cylinders-Vol 1: Fundamentals*, Oxford Univ. Press, New York, 1997.
[25] Vatsa, V. N., and Singer, B. A., "Evaluation of a Second-Order Accurate Navier-Stokes Code for Detached Eddy Simulation Past a Circular Cylinder," AIAA Paper AIAA-2003-4085, June 2003.
[26] Khorrami, M. R., Berkman, M. E., and Choudhari, M., "Unsteady Flow Computations of a Slat with a Blunt Trailing Edge," *AIAA Journal*, Vol. 38, No. 11, Nov. 2000, pp. 2050–2058.
[27] Khorrami, M. R., Singer, B. A., and Berkman, M. E., "Time-Accurate Simulations and Acoustic Analysis of Slat Free-Shear Layer," *AIAA Journal*, Vol. 40, No. 7, July 2002, pp. 1284–1291.
[28] Spalart, P. R., and Allmaras, S. R., "A One-Equation Turbulence Model for Aerodynamic Flows," AIAA Paper 92-0439, 1992.
[29] Couregelongue, J., "On the Existence of Two Families of Eddies Behind Immersed Solids," *Comptes Rendus Academie Sciences*, Vol. 189, Dec. 1929, pp. 972–974 (in French).

G. Candler
Associate Editor